Available online at www.sciencedirect.com

jmr&t Journal of Materials Research and Technology

journal homepage: www.elsevier.com/locate/jmrt

Original Article

Comparison of the combined oxidation and sulphidation behavior of nickel- and cobalt-based alloys at high temperature

Carlo Mapelli [a,*], Chiara Casalino [a], Andrea Strada [a], Andrea Gruttadauria [a], Silvia Barella [a], Davide Mombelli [a], Eugenio Longaretti [b], Francesco Perego [b]

[a] Dipartimento di Meccanica – Politecnico di Milano, Via La Masa 1, 20156 Milano, Italy
[b] FGS Fonderia Ghise e Acciai Speciali SpA, Via Garzoneri 11, 24047 Treviglio (BG), Italy

ARTICLE INFO

Article history:
Received 16 June 2020
Accepted 4 November 2020
Available online 20 November 2020

Keywords:
Nickel-based superalloy
Cobalt-based superalloy
Oxidation behavior
Sulphidation behavior

ABSTRACT

The combined oxidation-sulphidation behaviour at high temperature of two nickel-based and two cobalt-based cast alloys is analysed and discussed. These materials are evaluated in view of their possible application for building the components of the high temperature heating furnace up to 1380 °C. Typical service conditions combine extremely high temperatures with the simultaneous presence of sulphur-bearing impurities, due to the combustion of fuels derived from the coke production. The main requirements for this demanding application are simultaneous resistance to high thermal levels and to degradation caused by oxidation and sulphurization. The atmosphere chosen to simulate this harsh environment consists of atmospheric air enriched by 12% of sulphur. The testing procedure has been performed at three temperatures (1080 °C, 1180 °C and 1280 °C) and three times of exposure (24 h, 48 h and 96 h). Macroscopic observations have been coupled to microstructural investigations, performed by SEM-EDS. The analysis is mainly focused on the identification of the microstructural alterations experienced by each alloy and on the extent of internal attack caused by oxygen and sulphur. The combination of the macroscopic experimental data and the information from the microstructural observations alloys have been shown to point out the performances of alloy grade throughout the testing trials in order to define the chemical compositions associated to the moderate weight loss and limited depth of surface attack. The new chemical composition of a Ni-superalloy points out performance of corrosion resistance that are even better than the cobalt based alloys usually selected for such working conditions.

* *Corresponding author.*
E-mail address: carlo.mapelli@polimi.it (C. Mapelli).

https://doi.org/10.1016/j.jmrt.2020.11.009

1. Introduction

Heat-resistant nickel-alloys and cobalt-alloys are commonly employed to build the component for the furnaces and devices for heat treatments and for performing several metal forming processes at high temperature [1–4]: they combine excellent heat resistance and superior mechanical performances at high temperature. These features make them very eligible candidate materials for hot-work components like furnace riders, conveyor belts, transportation rolls and other tools. The durability of these components is strongly menaced not only by oxygen but also by the presence of sulphur compounds. The occurrence of high concentration of sulphur and of its compounds is in any high-temperature industrial environment. Coal, coke and other fossil fuels employed for combustion are in fact contaminated by extensive amounts of sulphur. Foundries and rolling mills often exploit residual sulphur-rich gases from the coke-oven installed nearby the combined-cycle thermoelectrical power plants, with a very negative impact on the durability of the equipment exposed to high temperature and severe atmosphere [5–7]. Sulphur gas compounds are dangerous for the health of the equipment because they are featured by high diffusivity and they manage to form low-melting eutectics especially with nickel [7,8] damaging the alloy. These issues acquire particular relevance in the field of materials selection, because both nickel and cobalt alloys are usually very expensive [9–11], and their adoption shall be justified and supported by a substantial increase in useful service life if compared to more conventional and cheaper heat-resistant steels. High-temperature degradation is a very alloy-specific phenomenon, where each class of metallic materials requires a customized treatment for an exhaustive assessment. The present study aims at assessing the response and durability of two Ni-based and two Co-based cast alloys, when exposed to a mixed oxidizing-sulphidizing atmosphere of fixed composition. In compliance with the reference real-case scenario, the atmosphere adopted for the tests is an oxidizing one. The field experience with similar service conditions has pointed out strong criticalities, even with alloys designed specifically for maximized heat and oxidation resistance [10,12–18].

2. Experimental procedure

All the materials have been supplied in the form of small casting ingots, featured by a diameter of 40 mm and 10 mm high. The compared chemical compositions have been selected in order to explore the answer of each grade usually applied in environment featured by aggressive environment and high temperature (Table 1).

Combined oxidation-sulphidation tests have been carried out in atmospheric air enriched by 12% H_2SO_4. The testing equipment consists of the refractory ceramic crucible built by ZrO_2 based refractory. The closed containers have been placed into an oven *Lenton UAF14/27 (UK)*, for three increasing time spans - 24 h, 48 h and 96 h.

The tests have been performed at three different temperatures: 1080 °C, 1180 °C and 1280 °C. Thus, the alloys have been tested at three levels of times and three temperature levels for a total of nine test conditions. Each experimental condition has been repeated three times, for a total of 27 samples.

After testing, samples have been mounted in phenolic or epoxy resin by a press, and prepared for the microstructural characterization through the standardized metallographic procedures, based on grinding (SiC paper discs, grit 120 to 2500) and polishing (colloidal diamond suspension, 6 μm–1 μm). After repeated rinses in ultrasonic bath with distilled water, the samples have been dried for at least 12 h with the aid of anhydrous colloidal silica. Micrographic investigation has been performed on the cross section of the samples by means of a W-filament scanning electron microscope (SEM) Zeiss EVO 50, both in secondary electron (SE) and back-scattered electron (BSE) modalities. Quantitative chemical analysis has been performed with an integrated Inca Oxford EDS (Energy Dispersive Spectrometer) probe. The specimens have also been analysed by an optical microscope after an etching of 10 s in a solution of 19 ml HCl + 1 ml H_2O_2.

3. Results

A preliminary observation of the microstructure featuring the coupons has been performed on the as-received materials and the analysis has pointed out a typical dendritic as-cast microstructure (Fig. 1).

All the alloys exhibit a sharp tendency to interdendritic segregation. Details of primary and secondary dendrite arm spacing, as well as dendrite length are reported in Table 2. Given the small dimension of the sand cast products, the grains are coarse, equiaxed and extremely large in size, in the order of magnitude of 10 mm. Conspicuous solidification defects (porosity, voids and micro-cracks) were detected in alloy 4 and, to a lesser extent, alloy 2.

In both nickel alloys (alloy 1 and alloy 2), the matrix is chiefly composed of γ' phase Ni_2Cr featured by a higher amount of tungsten in alloy 2, both in the matrix and more prominently in the interdendritic spaces. Combining the information from EDS analysis (Table 3) with data from suitable

Table 1 – Measured chemical compositions of the alloys, expressed in wt.%.

Alloy	C	Si	Mn	P	S	Cr	Ni	Mo	W	Fe	Co	Nb
Alloy 1	0.27	1.79	0.69	0.023	0.008	25.77	45.69	2.315	2.44	16.97	3.78	0.102
Alloy 2	0.18	1.61	0.79	0.019	0.007	26.91	43.93	0.405	9.12	14.05	2.63	0.052
Alloy 3	0.82	1.45	0.39	0.013	0.010	28.60	0.72	0.176	11.57	6.67	49.28	0.057
Alloy 4	0.14	1.27	0.32	0.013	0.007	27.91	1.01	0.230	2.21	16.97	49.45	0.271

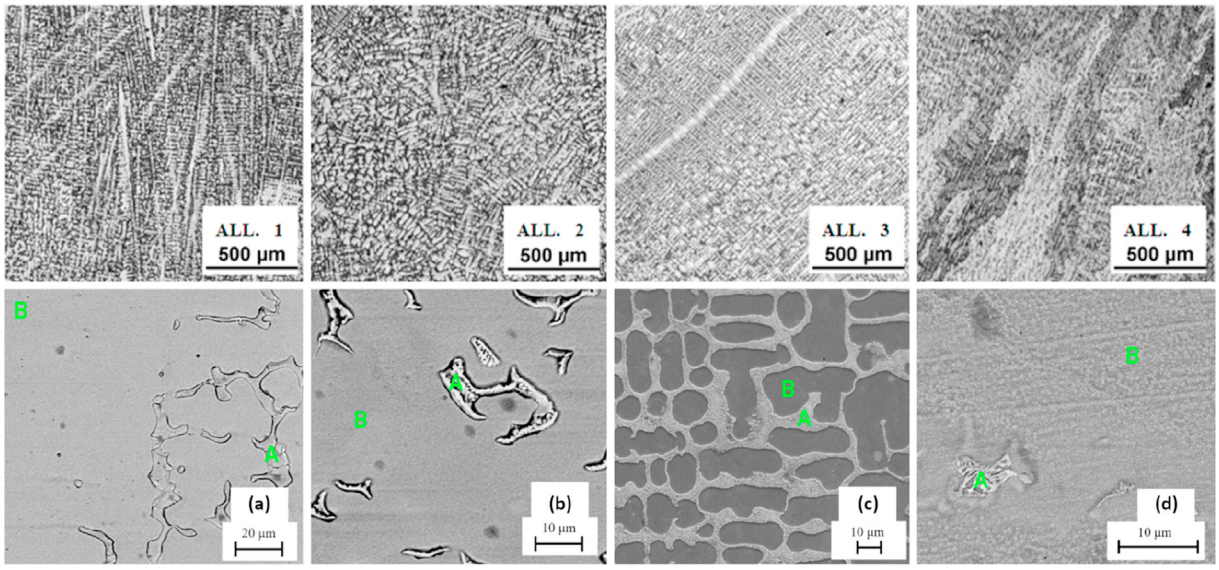

Fig. 1 – The observed microstructures from the left to the right side: alloy 1, alloy 2, alloy 3 and alloy 4. Upper line: optical microscopy images, lower line: scanning electron microscopy images.

Table 2 – Morphological features. All measurements in μm.

Alloy	PDAS	SDAS	Dendrite length
Alloy 1	100 ± 20	19 ± 2	670 ± 270
Alloy 2	140 ± 30	22 ± 3	470 ± 130
Alloy 3	45 ± 10	12 ± 1.5	500 ± 90
Alloy 4	37.5 ± 1.5	15 ± 0.5	1030 ± 250

binary and ternary alloy phase diagrams, it is possible to deduce the presence of well-defined intermetallic phases [4]:

- CrW, Ni_4Mo and ternary σ phase Ni–Cr–Fe in alloy 1;
- Ni_4W plus a mixed (αCr, W) phase in alloy 2.

Dendrites are extremely fine and columnar in both cobalt alloys. Both matrices are γ Co-rich solid-solution regions. Niobium segregation is well visible in alloy 4, where hypo-eutectic Nb–Co and hypereutectic Nb–Cr compounds have been detected from EDS analysis and binary alloy phase diagrams [4].

The mass variation experienced by each alloy as a function of the testing temperatures has been recorded (Fig. 2).

Mass variation at 1080 °C is modest for all the alloys and it becomes largely predominant for the long-term exposure, indicating the recurrent oxide detachments. There are no signs of distinction between the trends of nickel and cobalt alloys, since the latter class includes both the best performer (Alloy 3) and the sample that has experienced the highest mass loss (Alloy 4). The absolute value of the weight change generally increases through time with appreciable regularity.

Mass loss remains predominant also at 1180 °C. The response of Co-based alloy 3 and alloy 4 is sharply different. Alloy 3 points out a behaviour similar to both the Ni-based alloys. On the contrary, alloy 4 has experienced catastrophic degradation after 96 h, losing more than 60% of its initial mass. There is strong evidence of the inadequateness of alloy 4 at this service temperature. For the alloy 1 and alloy 2 the weight diminishes through time. Both alloys have provided optimal performances in the 96-h test.

At 1280 °C, the complete set of mass loss is available only for alloy 1 and alloy 2, whereas only short-term 24-h information is available for alloys 3 and alloy 4 because the degradation of the specimens for these two alloys has been so severe that the specimens have been fragmented. Both these Co-based alloys have proved a very quick oxidation when tested at 1280 °C just after an exposure of 24 h. A thick, cracked layer of unprotective scale has been observed on both alloys, determining significant mass gains. On the contrary, nickel alloys have in turn performed very well and they have been affected by moderate mass losses throughout the different time spans; thin, adherent, tenacious oxide layers protect the base metal from sulphur-induced degradation.

3.1. *Microstructure evolution for alloy 1*

The microstructure of alloy 1 after the exposure to the aggressive atmosphere has been observed after the application of the etching procedure (Fig. 3). The oxide layer is thin and inhomogeneous (Fig. 3(a)). The EDS analysis (Table 4) indicates that the formed layer is constituted mainly by Cr_2O_3 associated to NiO and SiO_2. This oxide system behaves as very adherent and have prevented further and deeper attack of the alloy 1 by the external agents. Some voids (Fig. 3(b) and eutectic low-melting phases (Fig. 3(d)) have been observed only after the high temperature exposure at the aggressive atmosphere and they have been not present in the as-cast condition. This phenomenon suggests that localized liquation phenomena and a following slow rate solidification phenomenon have occurred.

Sulphides have been detected as small particles dispersed within the metal matrix (Table 5). Sulphur

Table 3 – SEM-EDS analysis of alloy 1–4 in Fig. 1.

% by weight	Point	phase	O	Si	Cr	Mn	Fe	Co	Ni	Nb	Mo	W
Alloy 1	(a) – A	σ-phase		2.87	42.41	0.68	8.63	1.79	21.07		13.92	8.64
	(a) – B	γ′		1.84	25.47	1.07	17.16	3.09	44.29		3.60	3.48
Alloy 2	(b) – A	αCr,W			40.57	0.62	5.09	1.24	14.28		3.38	34.82
	(b) – B	γ′	2.77		24.63	0.58	16.67	2.70	40.05			12.60
Alloy 3	(c) – A	γ-Co + M_xC_y		0.49	38.30	1.03	3.89	34.36				21.93
	(c) – B	γ-Co		0.72	25.79	0.68	6.40	55.42				10.98
Alloy 4	(d) – A	Nb–Co/Cr	0.66	4.00	27.69	0.17	11.76	30.52		24.78		0.41
	(d) – B	γ-Co		0.69	26.56	0.30	19.76	49.64				3.05

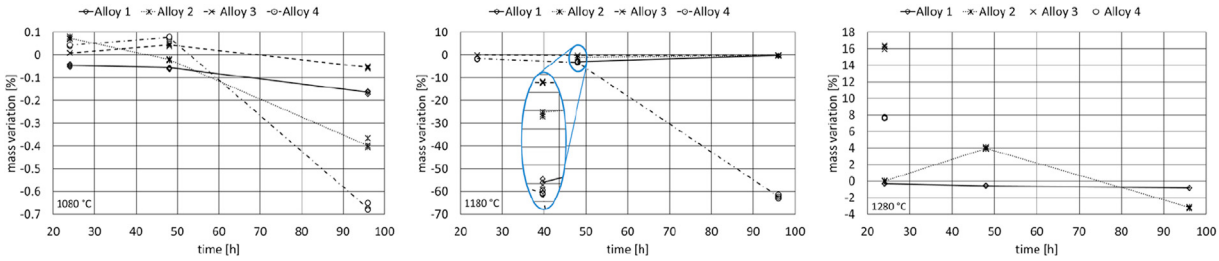

Fig. 2 – Weight change at 1080 °C, 1180 °C, and 1280 °C of the four alloys after three-time ranges.

diffusion has followed a precise scheme under all testing conditions, exploiting the cracks in the oxide scale and the interdendritic pattern inside metal matrix. From a morphologic point of view, the sulphides (Fig. 3(b)) are present in the form of globular particles - seldom acicular, more elongated and whisker-like. Sulphides are small in size, namely the 97% of the sulphide particles are featured by a diameter of 1–4 μm in most cases, and no particle featured by a diameter higher than 10 μm has been observed in alloy 1 (Fig. 4).

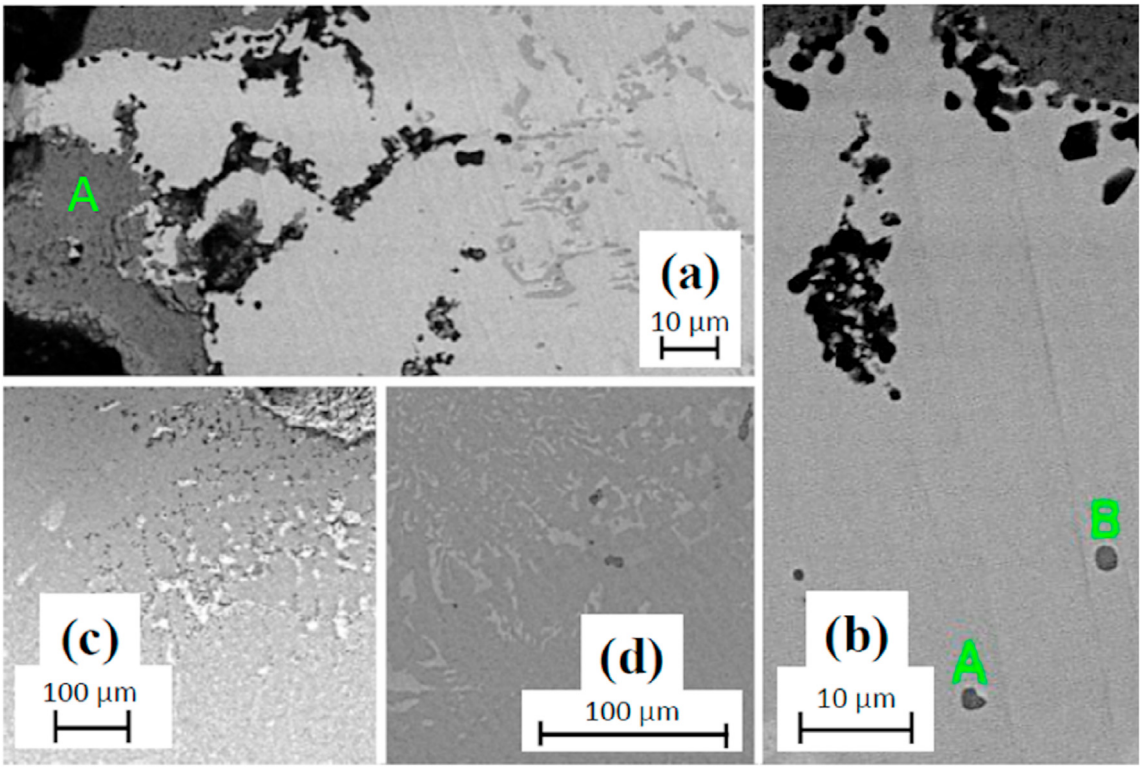

Fig. 3 – SEM micrographs of alloy 1: (a) after 48 h at 1080 °C; (b) after 48 h at 1080 °C; (c) after 24 h at 1180 °C; (d) after 96 h at 1280 °C.

Table 4 – SEM-EDS analysis of alloy 1 in Fig. 3.

% by weight	O	Si	S	Cr	Mn	Fe	Ni
3(a) A	21.56	6.34		69.76			2.35
3(b) A		1.57	27.53	31.36	25.83	3.41	10.30
3(b) B			25.51	35.71	16.77	6.10	15.91

The interdendritic pattern is the preferential path of diffusion for both oxygen and sulphur.

3.2. *Microstructure evolution for alloy 2*

The alloy 2 has been affected by a mild mass loss featured by a moderate corrosion depth, below 1.5 mm for both oxidation and sulphidation.

The analysis performed on alloy 2 highlights the formation of a thin, homogeneous oxide layer. Also The scale still consists of a mixture of Cr_2O_3, Fe_2O_3, NiO, MnO (Table 6). Alloy 2 has seldom undergone oxide detachment that takes place when the layers achieved a thickness of 2–4 mm, because it becomes brittle and fragmented.

The local melting and solidification phenomena have taken place at the grain boundaries, as proved by the presence of eutectic low-melting phases and voids, not present in as-cast condition. The presence of lamellar eutectics affects the whole bulk material. The porosities have absented before the corrosion tests and have emerged after those, so they are consequence of local liquation phenomena due to the presence of low-melting compounds formed by the sulphur action (Fig. 5).

Figure 6(a) and (b) indicates clearly that the interdendritic regions are the preferential path for the diffusion of the etching elements, especially sulphur. The sulphides are small and globular and the sulphur is concentrated at the grain boundaries or at of the lamellar eutectics (Fig. 6(c)). On the contrary, sulphur has not been detected in chromium-rich metallic phases present in the metal matrix (Table 7).

Significant amounts of oxygen have managed to enter the base metal, following an interdendritic pattern despite the presence of the oxide scale layer. The dendritic profile is neat, and it is clearly recognized from the micrographs. Micro-scale shrinkage voids and segregation phenomena has taken place (Fig. 6(e)).

3.3. *Microstructure evolution for alloy 3*

The observations reveal the formation of non-homogenous oxide layers, formed mainly by Cr_2O_3, Fe_2O_3, Co_3O_4 and SiO_2. Oxide detachment has seldom been observed. The maximum depth of the affected zone 1 mm (Table 8).

Owing to the severe testing conditions, at grain boundaries some eutectic compounds have nucleated (Fig. 7(e)) during the test trials. For long testing times, other eutectic domains have grown (Fig. 7(b)). The presence of eutectic low-melting phases implies that, a slow rate solidification phenomenon has taken place during the cooling. The morphology of the eutectic is lamellar, and it is three component alloy formed by Co–Cr–W. The presence of $(Co,Cr)_7W_6$ has been confirmed by EDS analysis for the bright phases of Fig. 9(b) (A mark), and Co_3W and $(Co,Cr)_7W_6$ have been identified by EDS analysis in Fig. 9(e) (E mark) (Table 8).

Below the scale an extensive region affected by the damaging phenomena are clearly visible (Fig. 8). The external oxide scale is thick and apparently well adherent, but it is also prone to become less protective than the layer formed by alloy 1 and alloy 2. Moreover, once the degradation mechanism has been triggered, the very peculiar structure of this Co-based alloy - consisting of fine, columnar dendrites - creates very favourable conditions to the extensive internal penetration of both oxygen and sulphur, giving rise to fairly deep internal attacks (Table 9). The morphology of sulphides is featured by sharp and significant differences with respect to Ni-based alloys. Actually, the sulphides are not only globular but also continuous and elongated along the interdendritic spaces. The length of such phases achieves up to 50 μm (Fig. 8(b)). at the lowest testing temperature the sulphides have also been detected as tiny, whisker-like acicular particles (Fig. 8(a)), very close to the interface between lamellar eutectic structures and the metal matrix and they have been featured by sizes ranging from 10 μm up to 15 μm.

3.4. *Microstructure evolution for alloy 4*

The observed oxides (Fig. 9) are thick, inhomogeneous and very mixed and formed primarily by a mixture of CrO_3, Fe_2O_3, Co_3O_4, SiO_2 - notice that chromium oxide is far from being the dominant constituent in most cases (Table 10). The oxide detachment has been recurrent and severe, with extensive metal loss. The affected zone can achieve 2 mm at 1280 °C even for only 24 h. The morphology of the eutectic phases is lamellar, and it comes from a triphasic alloy of Co–Cr–Fe. The presence of Cr+σ phase can be derived from the results of EDS analysis (Table 10).

Focusing on long-term exposure data, the comparison among the micrographs (Fig. 10) and EDS analysis (Table 11) indicates that the Co-based matrix is very rich in globular sulphide particles (32.46 wt.% S in point A), and tiny needle-

Table 5 – SEM-EDS analysis of alloy 1 in Fig. 4.

% by weight	O	Al	Si	S	Cr	Mn	Fe	Ni	Mo	W
4(a) A		4.36	2.60	7.84	46.22	12.03	3.27	14.21		8.91
4(b) A				36.39	23.50	40.11				
4(b) B			6.54		25.52		2.52	27.36	24.93	13.14
4(b) C				37.81	25.59	36.60				
4(c) A	6.16		11.54	21.38	24.65	16.47	3.84	15.97		
4(c) B				38.66	23.58	37.75				

shaped metallic phases extremely rich in chromium (up to 89.37 wt.% Cr) has been detected in these domains. The formation of these phases has depleted the base metal from an extensive amount of chromium to be exploited for selective oxidation, with a strong acceleration in both the kinetics and the extent of the attack (less protective, Co-rich and Cr-poor oxide scale) [19,20]. The detected sulphides are either globular or slightly acicular; their scattered location shall be mainly ascribed to the extensive development of the interdendritic regions. In Fig. 10(c), sulphur has managed to diffuse

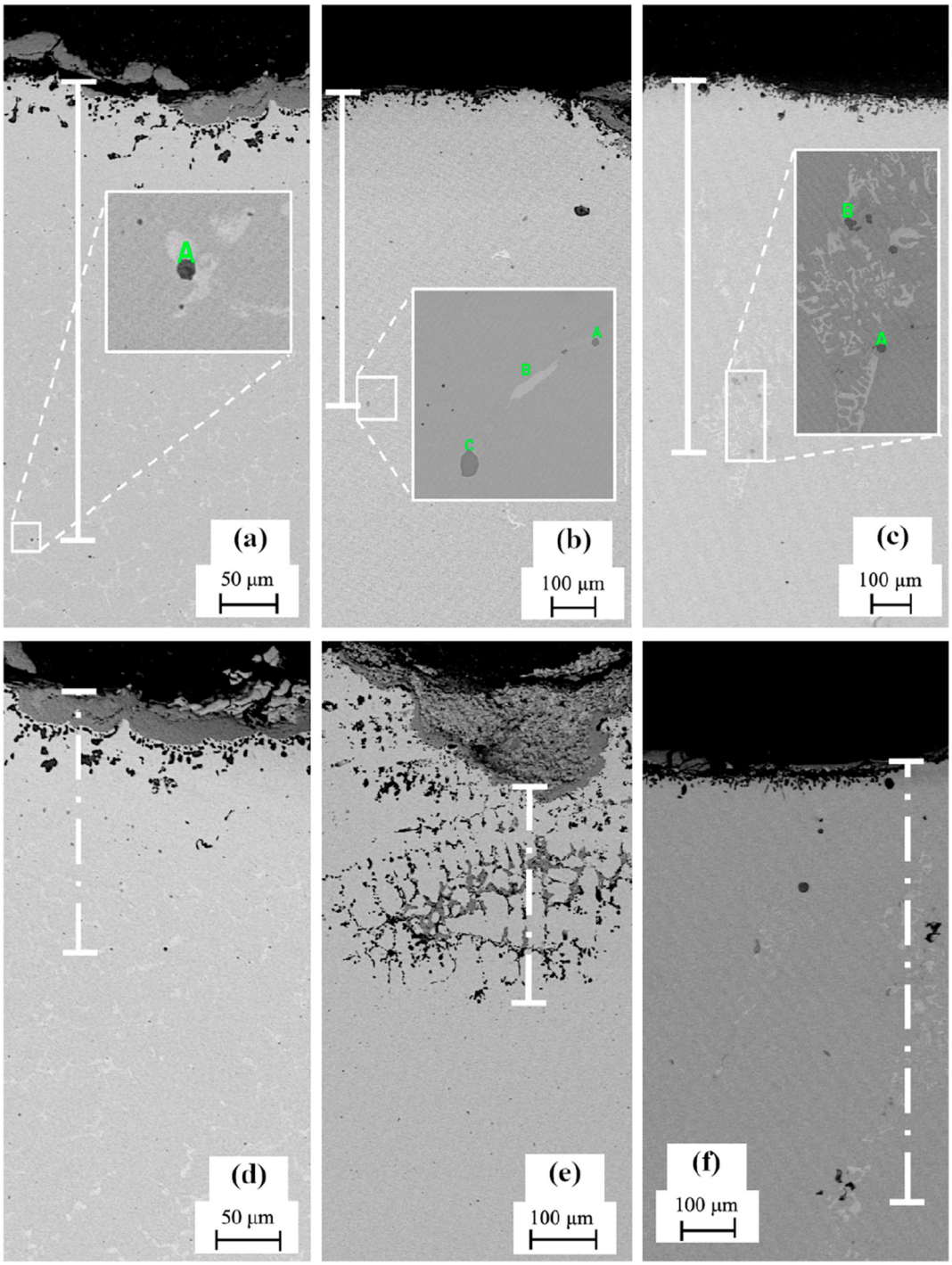

Fig. 4 – Observed depth of diffusion of sulphur (continuous line) and oxygen (dashed lines) in alloy 1: (a) distance equal to 410 ± 15 μm at 1080 °C; (b) distance equal to 719 ± 25 μm at 1180 °C; (c) distance equal to 964 ± 85 μm at 1280 °C; (d) distance equal to 209 ± 7 μm at 1080 °C; (e) distance equal to 342 ± 13 μm at 1180 °C; (f) distance equal to 816 ± 35 μm at 1280 °C.

Table 6 – SEM-EDS analysis of alloy 2 in Fig. 5.

% by weight	O	Si	S	Cr	Mn	Fe	Ni
oxide layer	16.98	5.97	0.69	42.45	11.41	10.53	10.19
5(a) A		1.57	27.53	31.36	25.83	3.41	10.30
5(b) B			25.51	35.71	16.77	6.10	15.91
5(c) A			25.50	30.33	30.39	5.18	

along a three-sided path, consisting of porosity in the oxide scale.

4. Discussion

Evidence of casting and solidification defects observed in the sample of alloy 4 suggests that this alloy will be more prone to an accelerated degradation, because larger pathways are available for the internal penetration of both oxygen and sulphur. These foundry defects must be taken into account in the discussion of the results, because they are supposed to alter the response of this alloy.

At 1080 °C the spallation effect rules the weight loss of the studied alloys that take place because the oxide growth becomes unstable at a certain stage due to the large thickness of the formed oxide layers.

Both Co-based alloys have pointed out a very quick oxidation when tested at 1280 °C just after an exposure of 24 h. The formation of a thick and non protective scale has been observed on both the alloys, and this has determined a significant mass loss. On the contrary, nickel alloys have performed very well, with moderate mass losses throughout the different time spans even at 1280 °C. The good performance of the Ni-based alloys is the consequence of the formation of thin, adherent, tenacious oxide layers that protect the metal matrix from the sulphur-induced degradation. The formation of such a protective oxide layer is more pronounced for alloys 1 than for alloy 2 and this is the reason why alloy 2 shows a higher degradation rate measured by the weight loss.

Moreover, once the degradation mechanism has been triggered, it seems that the very peculiar structure of this Co-based alloy - consisting of fine, columnar dendrites - creates very favourable conditions to the extensive internal penetration of both oxygen and sulphur, giving rise to fairly deep internal attacks. The elongated sulphide phases formed in the interdendritic spaces Co-based alloys promotes the instability and the detachment of the layers forming on the surface.

Moreover, the worst resistance behaviour pointed out by alloy 4 is a consequence of the simultaneous presence of a wide development of the interdendritic pattern and the depletion of the Cr of the metal matrix due to the precipitation of the phases of intermetallic compounds involving such a chemical element that cannot participate to the formation of the protective oxide layer.

The more adhesive behaviour of the oxide layer formed on the Ni-based alloys and their coarser dendrite structure

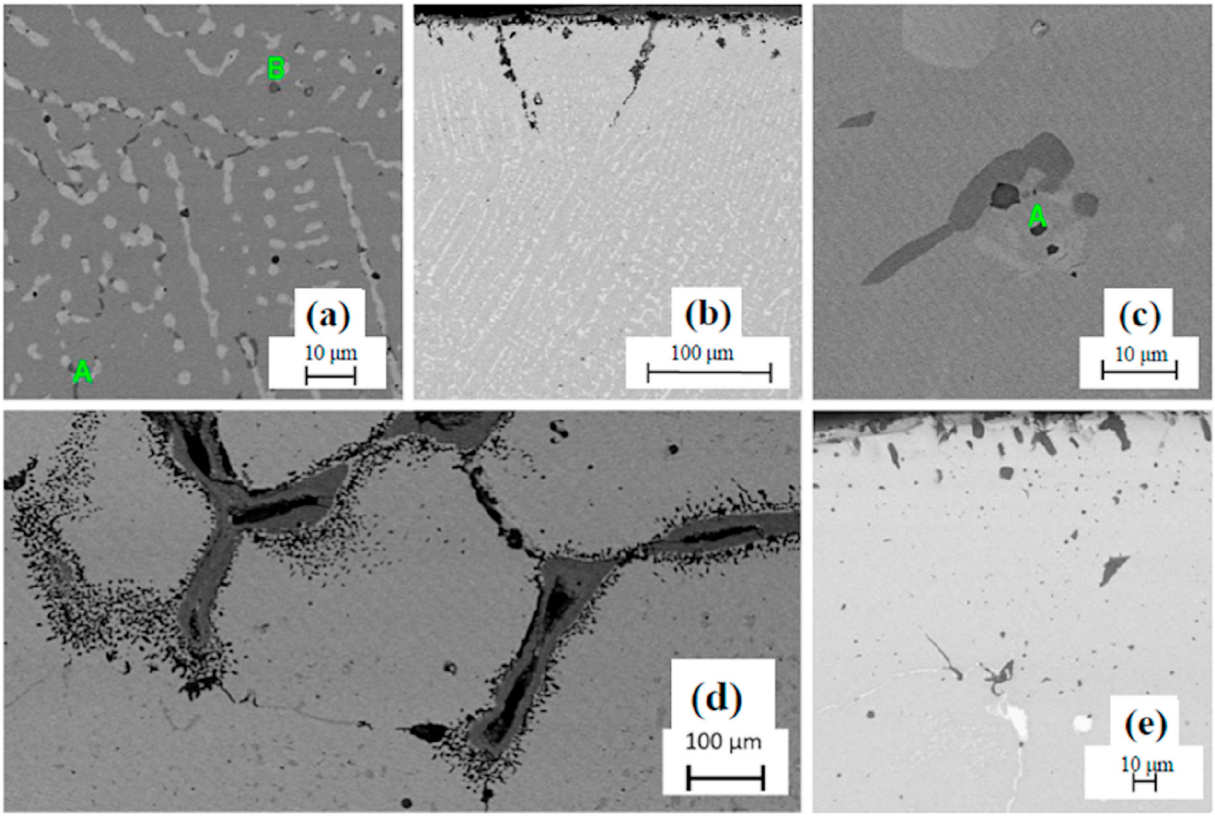

Fig. 5 – SEM micrographs of alloy 2: (a) after 48 h at 1080 °C; (b) after 96 h at 1080 °C; (c) after 48 h at 1180 °C; (d) after 96 h at 1180 °C; (e) after 24 h at 1280 °C.

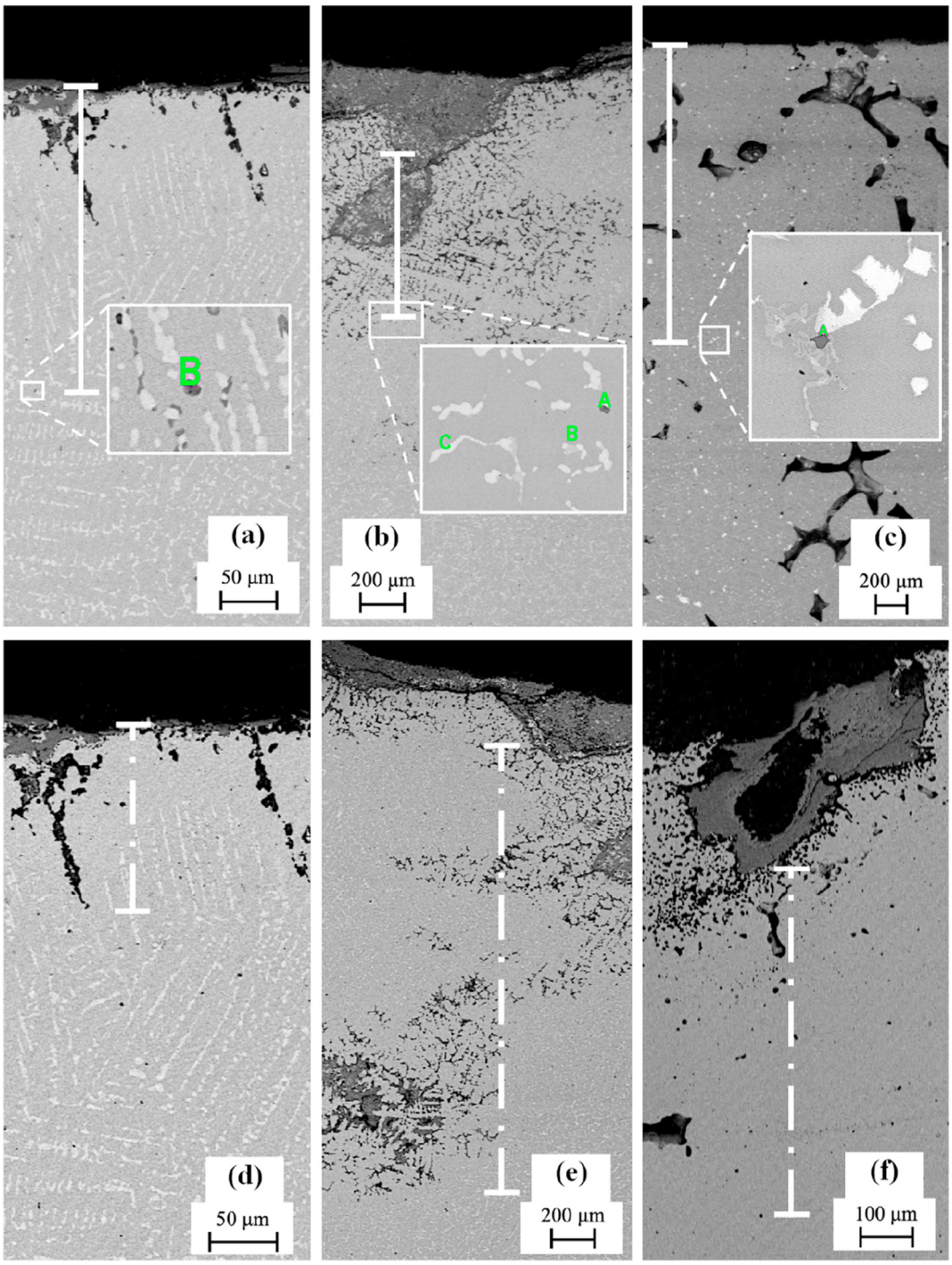

Fig. 6 – Observed depth of diffusion of sulphur (continuous line) and oxygen (dashed lines) in alloy 2: (a) distance equal to 275 ± 17 μm at 1080 °C; (b) distance equal to 725 ± 22 μm at 1180 °C; (c) distance equal to 1733 ± 68 μm at 1280 °C; (d) distance equal to 140 ± 19 μm at 1080 °C; (e) distance equal to 1840 ± 35 μm at 1180 °C; (f) distance equal to 663 ± 28 μm at 1280 °C.

Table 7 – SEM-EDS analysis of alloy 2 in Fig. 6.

% by weight	Al	S	Ca	Cr	Mn	Fe	Co	Ni	Nb	W
6(a) B		20.04	1.38	22.53	15.88	10.47	2.34	23.39		3.97
6(b) A	0.97	26.89	4.00	19.18	28.71	3.00		11.00		6.24
6(b) B				63.19		4.76		5.18		26.87
6(b) C		0.23		25.16		3.73		23.79	2.35	44.75
6(c) A		37.45		30.20	32.35					

Table 8 – SEM-EDS analysis of alloy 3 in Fig. 7.

% by weight	O	Si	S	Cr	Mn	Fe	Co	Ni	Ta	W
oxide layer	14.19	2.59		36.99	1.23	4.02	33.50			
7(a) A			40.32	35.59	24.09					
7(a) B				35.81		4.25	37.80			22.15
7(a) C				13.83			27.22			58.95
7(a) D				25.21		2.59	32.11			40.09
7(b) A				5.94		2.29	20.11			71.66
7(b) B				11.27		3.07	24.43			61.22
7(b) C			36.96	33.19	29.86					
7(b) D				82.24			10.46			7.30
7(b) E				27.01		3.79	39.21			29.99
7(b) F				47.48		1.85	26.62		3.86	20.18
7(c) A			15.84	25.79	11.91	4.10	35.89			6.47
7(d) A		1.45	40.20	58.35						
7(d) B		9.16	37.73	53.11						
7(d) C		1.57	25.22	32.25	15.68	2.11	23.18			
7(e) A	24.08	34.28		6.56		2.17	32.91			
7(e) B	17.31			82.69						
7(e) C	20.09	22.09		33.65			13.40			10.76
7(e) D				4.43		1.93	54.03	14.05		25.56
7(e) E				11.01		2.84	38.47			47.69
7(e) F	25.50	39.26		8.57		2.03	24.64			

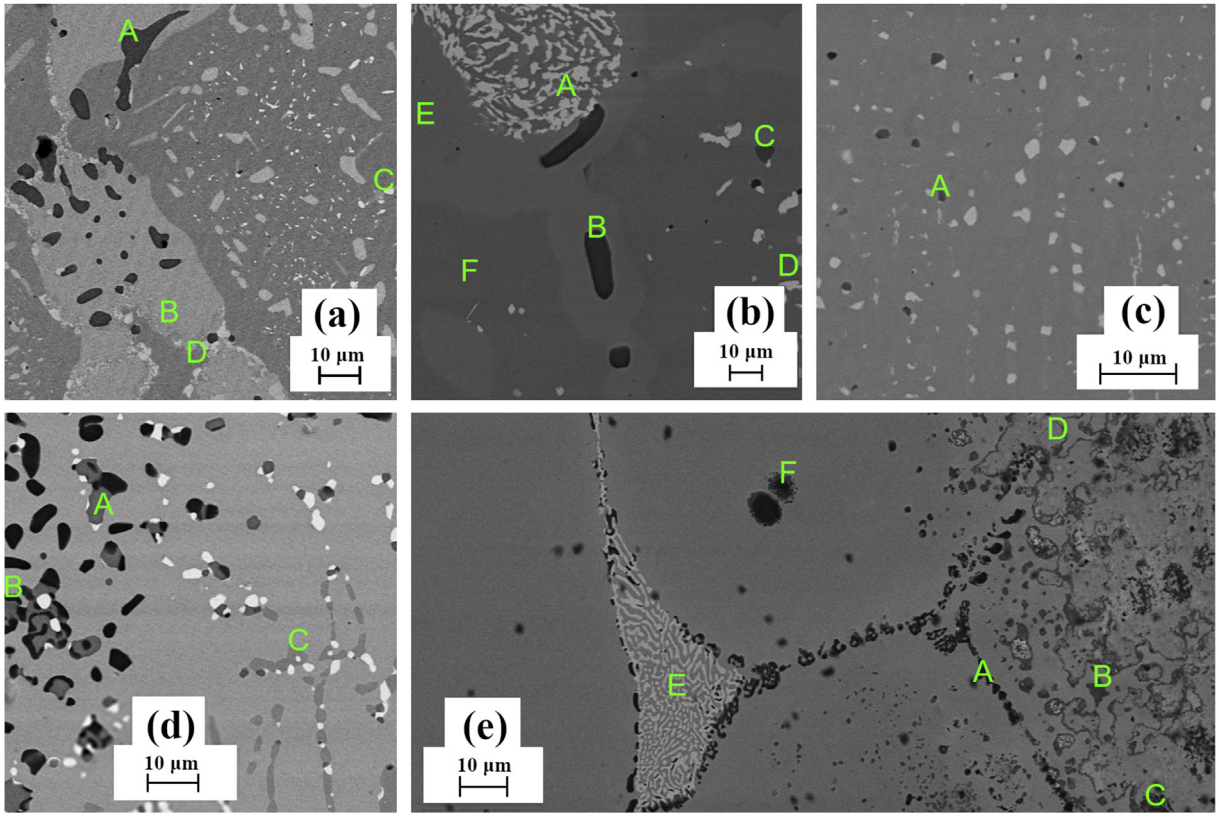

Fig. 7 – SEM micrographs of alloy 3: (a) after 96 h at 1080 °C; (b) after 96 h at 1080 °C; (c) after 48 h at 1180 °C; (d) after 96 h at 1180 °C; (e) after 24 h at 1280 °C.

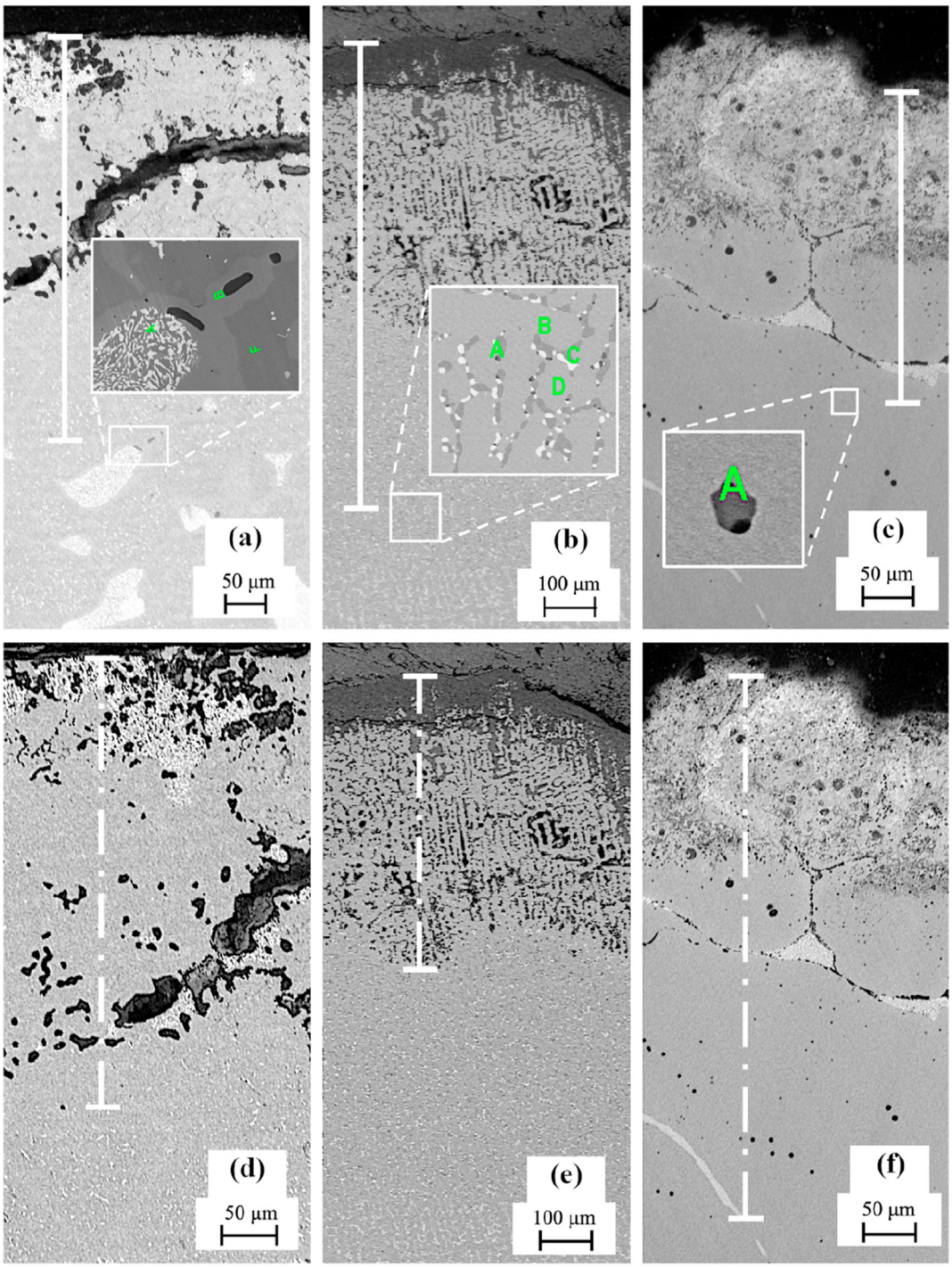

Fig. 8 – Observed depth of diffusion of sulphur (continuous line) and oxygen (dashed lines) in alloy 3: (a) distance equal to 507 ± 20 μm at 1080 °C; (b) distance equal to 934 ± 31 μm at 1180 °C; (c) distance equal to 308 ± 11 μm at 1280 °C (d) distance equal to 398 ± 17 μm at 1080 °C; (e) distance equal to 550 ± 12 μm at 1180 °C; (f) distance equal to 536 ± 24 μm at 1280 °C.

(featured by a short development of the interdendritic patterns – Table 2) than the Co-based alloys induce the best high temperature corrosion resistance behaviour shown by the Ni-based alloys. This is a novelty point if compared to the usual design approach that favours the Co-based alloys at the expense of the Ni-based alloys in high temperature, oxidizing and sulphidizing environment, because the obtained results indicated that Ni-based alloys featured by a coarse dendrite microstructure are more reliable than Co-based alloys in that environment.

The worse performance of the alloy 2 than alloy 1 is a consequence of the more pronounced and thicker

Table 9 – SEM-EDSs analysis of alloy 3 in Fig. 8.

% by weight	O	Cr	Mn	Fe	Co	Ta	W
8(a) A		5.94		2.29	20.11		71.66
8(a) B		11.27		3.07	24.43		61.22
8(a) F		47.48		1.85	26.62	3.86	20.18
8(b) A	20,47	44.17	15.19		9.93		
8(b) B		85.24			3.85		
8(b) C		15.63		2.64	22.32		
8(b) D		23.30		6.82	59.00		

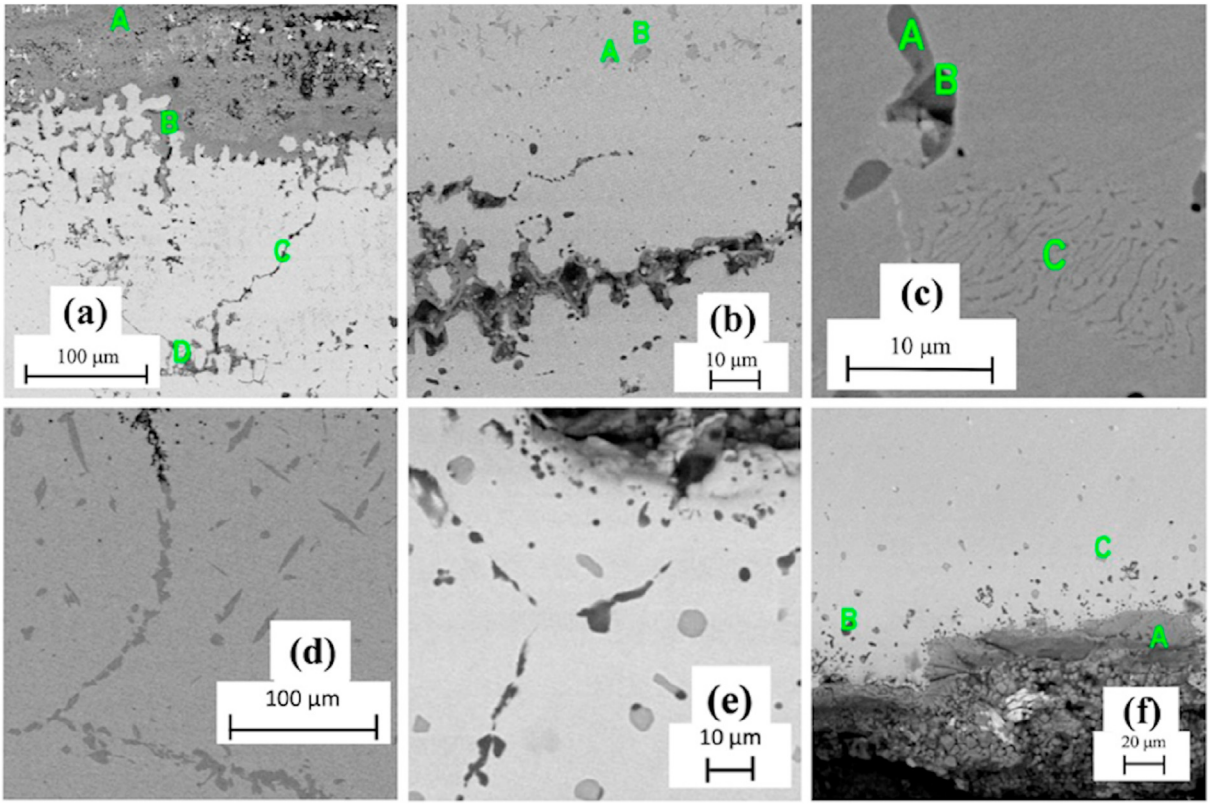

Fig. 9 – SEM micrographs of alloy 4: (a) after 48 h at 1080 °C; (b) after 48 h at 1080 °C; (c) after 48 h at 1180 °C; (d) after 96 h at 1180 °C; (e) after 24 h at 1280 °C; (f) after 24 h at 1280 °C.

Table 10 – SEM-EDS analysis of alloy 4 in Fig. 9.

%by weight	O	Si	S	Cr	Mn	Fe	Co	W
oxide layer	21.09	2.20	0.17	45.16	4.76	8.85	9.17	
9(a) A	18.54			16.60		25.67	39.18	
9(a) B	14.27	3.73		13.26		9.39	43.17	16.20
9(a) C				16.56		22.83	57.62	2.98
9(a) D	28.75	21.26		38.46		2.66	8.88	
9(b) A		2.42	6.12	23.43	3.73	19.20	45.10	
9(b) B			0.95	92.81			2.93	3.30
9(c) A	1.80	1.32		96.88				
9(c) B		1.30	25.02	20.50	28.63	6.87	17.66	
9(c) C		0.35	0.09	27.91		20.23	47.47	
9(f) A	17.03			80.32				
9(f) B	20.22	41.02		6.88		9.13	22.75	
9(f) C			32.23	51.30	9.33	1.98	5.16	

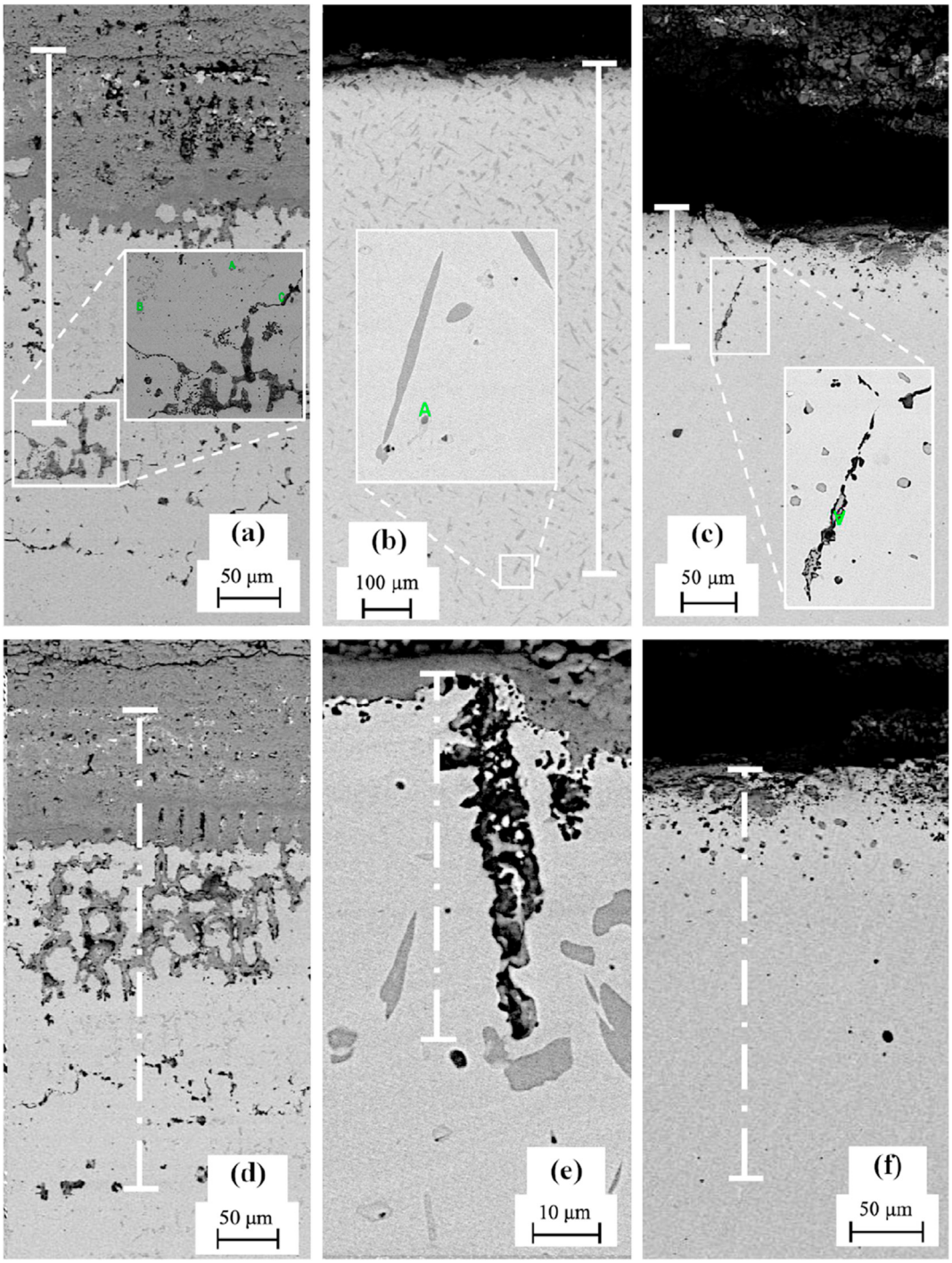

Fig. 10 – Observed depth of diffusion of sulphur (continuous line) and oxygen (dashed lines) in alloy 4: (a) distance equal to 305 ± 8 μm at 1080 °C; (b) distance equal to 1047 ± 29 μm at 1180 °C; (c) distance equal to 135 ± 7 μm at 1280 °C(a) distance equal to 400 ± 22 μm at 1080 °C; (b) distance equal to 58 ± 4 μm at 1180 °C; (c) distance equal to 291 ± 11 μm at 1280 °C.

Table 11 – SEM-EDS analysis of alloy 4 in Fig. 10.

% by weight	O	Si	S	Ti	Cr	Mn	Fe	Co
10(a) A			26.89		35.05	15.59	6.88	15.59
10(a) B					71.85		9.19	18.96
10(a) C	17.77	32.94			10.25		10.79	28.25
10(b) A			22.75		36.36	31.78	2.98	6.13
10(c) A	5.58	8.28	32.04		47.75		2.07	4.29

interdendritic pattern featuring alloy 2. Actually, in all the observed samples the extent of the interdendritic pattern and of the segregation is the ruling factor that promotes the diffusion phenomena of oxygen and sulphur at high temperature.

5. Conclusions

The combined oxidation-sulphidation behaviour of two Ni-based cast alloys and two Co-based cast alloys has been investigated and discussed under nine different combinations of time and temperature, in atmospheric air enriched by 12% H_2SO_4. The study aims at providing quantitative results about mass variation and internal diffusion of critical species. From the experimental results of the tests and on the basis of the performed microstructural characterization, the following conclusions can be stressed:

- mass loss is largely predominant on mass gain for all the alloys, indicating a generalized tendency to spallation effects arising from thermal and mechanical stresses in the oxide layer. Only Co-based alloy 3 and alloy 4 have largely increased in mass after 24 h at 1280 °C. Alloy 4 has undergone catastrophic oxidation after 96 h at 1180 °C;
- not only the chemical composition is fundamental for the corrosion resistance but also the development of the interdendritic pattern plays a fundamental role: high PDAS, SDAS and short dendrite length led lower the diffusion of oxygen and sulphur inside the alloys.

For this reason:

- the corrosion resistance of the Co-based alloys is affected by the fine dendritic structure and by the significant development of the interdendritic patterns that promotes the diffusion oxygen and sulphur in the subsurface layers; leading the formation of elongated sulphur compounds that undermines the stability of the oxide layer that becomes prone to the spallation phenomenon;
- the best high temperature corrosion resistance behaviour is associated to the alloy 1 featured by the highest Ni concentration: the protective and adherent layer formed during the test and the coarse dentritic structure prevent the O and S diffusion giving rise to the less mass losses.

Funding

This research did not receive any specific grant from funding agencies in the public, commercial, or not-for-profit sectors.

Author's contribution

Carlo Mapelli: Conceptualization. **Andrea Gruttadauria**: Resources. **Silvia Barella**: supervision. **Davide Mombelli**: Writing – Original draft. **Andrea Strada, Chiara Casalino**: Investigation, Formal analysis. **Eugenio Longaretti, Francesco Perego**: Methodology, Supervision.

Data availability

The raw/processed data required to reproduce these findings cannot be shared at this time as the data are confidential and also forms part of an ongoing study.

Declaration of Competing Interest

The authors declare that they have no known competing financial interests or personal relationships that could have appeared to influence the work reported in this paper.

REFERENCES

[1] Khanna AS. High temperature oxidation. Handb. Environ. Degrad. Mater.. Elsevier; 2005. p. 127–94.
[2] Smith RA, Sauders SRJ. Nickel and its alloys. Third Edit. In: Shreir LL, Jarman RA, Burstein GT, editors. Corros. 3rd ed., vol. 1. Oxford: Butterworth-Heinemann; 2013. p. 7. https://doi.org/10.1016/B978-0-08-052351-4.50062-5. 91-97:144.
[3] Lai GY. High-temperature corrosion and materials applications. ASM international; 2007.
[4] Davis J. Uses of nickel. Materials Park, Ohio: ASM International; 2000. https://doi.org/10.1361/ncta2000p013.
[5] Pond RB, David A. High-temperature corrosion-related failures. Fail Anal Prev 2002;11:868–80.
[6] Birks N, Meier GH. Introduction to high temperature oxidations of metals, vol. 17. London: Edward Arnold Ltd; 1983. p. 1995.
[7] Cramer SD, Covino BSJ, editors. ASM handbook volume 13A: corrosion: fundamentals, testing, and protection. Materials Park, Ohio: ASM International; 2003.
[8] Kelly JC, Wilson JD. Oxidation rates of some heat resistant alloys. 1995.
[9] Buscail H, Rolland R, Riffard F, Issartel C, Perrier S. Cobalt based alloy oxidation at high temperatures. 2013.
[10] Clark CC, Hulsizer WR. The long-term, cyclic-oxidation behavior of selected chromia-forming alloys. Oxid Met 1998;49:373–99.
[11] Grubb JF. Pickling and surface chromium-depletion of corrosion-resistant alloys. In: Int. Conf. Stainl. Steels. Chiba: The Iron and Steel Institute of Japan; 1991. p. 944–51.
[12] McCarron RL, Schultz JW. High temperature gas-metal reactions in mixed environments. 1973.
[13] Wuchina E, Opila E, Fergus J, Maruyama T, Shifler D. High temperature corrosion and materials chemistry. Electrochem. Soc.; 2009.
[14] Asteman H, Svensson J-E, Johansson L-G, Norell M. Indication of chromium oxide hydroxide evaporation during oxidation of 304L at 873 K in the presence of 10% water vapor. Oxid Met 1999;52:95–111.
[15] Shatynski SR. The thermochemistry of transition metal sulfides. Oxid Met 1977;11:307–20.
[16] Baker H. ASM handbook: alloy phase diagrams, vol. 3. Ohio: ASM international Materials Park; 1992.
[17] Perkins R. Current status of alloy design for high temperature corrosion resistance. Environ Degrad High Temp Mater 1980;2:5.

[18] Clark CC, Hulsizer WR. Superalloys development for gas turbines operating in the marine environment. In: Miler CL, editor. Gas turbine mater. 1972 conf. Hyattsville: Naval Ship Engineering Center; 1972. p. 35–42.
[19] Soltanar S. High temperature corrosion behavior of alloys in mixed gas environments. University of Pittsburgh; 2018.
[20] Grabke H, Petersen E, Srinivasan S. Influence of adsorbed sulfur on surface reaction kinetics and surface self-diffusion on iron. Surf Sci 1977;67:501–16. https://doi.org/10.1016/0039-6028(77)90011-5.